Journal of Sound and Vibration (1999) **220**(5), 787–806
Article No. jsvi.1998.1933, available online at http://www.idealibrary.com.on IDEAL

A TWO-DIMENSIONAL AXISYMMETRIC NUMERICAL ANALYSIS OF A BAR–BAR TENSILE IMPACT APPARATUS BY ELASTOPLASTIC FEM

C. Y. Wang, H. P. Wan and Y. M. Xia

Department of Modern Mechanics,
University of Science and Technology of China, *Hefei*, *Anhui* 230027,
People's Republic of China

(*Received* 3 *September* 1997, *and in final form* 14 *August* 1998)

At present, a bar–bar Tensile Impact Apparatus (BTIA) is widely used to measure the dynamic tensile properties of solid materials. A BTIA consists of two long bars, between which a specimen is connected. Hence, there are several physical and geometric discontinuous sections in a BTIA. In the present paper, a two-dimensional axisymmetric elastoplastic finite element model for a BTIA with a dumb bell-shaped cylindrical specimen is established. The numerical solution for the model is solved by ADINA. In the scope of elastoplastic theory, the numerical analysis confirms the validity of the 1D experimental measuring principle of BTIA, so long as certain foundations are satisfied. The effects of the specimen geometry and strain rate are also discussed. The matching relation between the specimen and the BTIA system has been studied.

1. INTRODUCTION

1.1. BAR–BAR TENSILE IMPACT APPARATUS (BTIA), 1D EXPERIMENTAL PRINCIPLE

Since Kolsky [1] first developed the modern Split Hopkinson Pressure Bar (SHPB) apparatus in 1949 on the basis of a great quantity of previous work, tremendous progress has been made in the measurement of materials at high rates of strain. In the 1960's and 1970's, a number of researchers conducted a large amount of theoretical and experimental research work in order to improve the BTIA technique and extend its usage. Bertholf [2] and Bertholf and Karnes [3] produced a two-dimensional axisymmetric numerical analysis for SHPB. They studied the influences on the experimental results of the specimen geometry and the friction between the specimen and input/output bar, and gave the matching relation between the specimen and the SHPB system that made the experimental measuring principle valid under small friction. Bertholf's work laid a solid theoretical foundation for the SHPB technique.

0022–460X/99/100787 + 20 $30.00/0

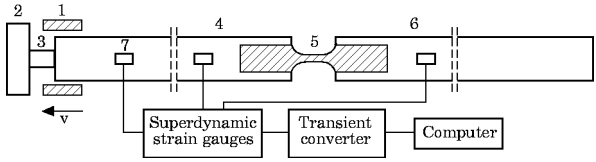

Figure 1. Sketch of bar–bar tensile impact apparatus: 1 hammer, 2 block, 3 short metal bar (made of aluminium alloy), 4 input bar, 5 specimen, 6 output bar and 7 strain gauges.

In recent decades, various tensile impact apparatuses have been developed one after another. The bar–bar tensile impact apparatus is the chief form. Y. M. Xia *et al*. [4] developed the rotation disk tensile impact test apparatus. As shown in Figure 1, when the hammer on the high-speed rotation disk (the disk is not shown in the figure) impacts on the block, the short metal bar (made of aluminium) is broken, which produces an approximately rectangular input stress impulse wave. Making use of the plastic flow of the short metal, the oscillation in the incident impulse, compared with the general way of using the hammer to impact directly on the block, is filtered a great deal. This technique can make the incident impulse very smooth, which enhances the accuracy of experimental results.

The experimental measuring principle of BTIA is the same as that of SHPB when ignoring the difference of the incident impulse between BTIA and SHPB. The principle can be expressed by the sketch of Lagrange X-T (shown in Figure 2), which is based on the assumptions (1) stress wave propagations in the input/output bar are elastic and one-dimensional, (2) the stress and strain fields in the specimen must be uniform and must be under a unidirectional stress state.

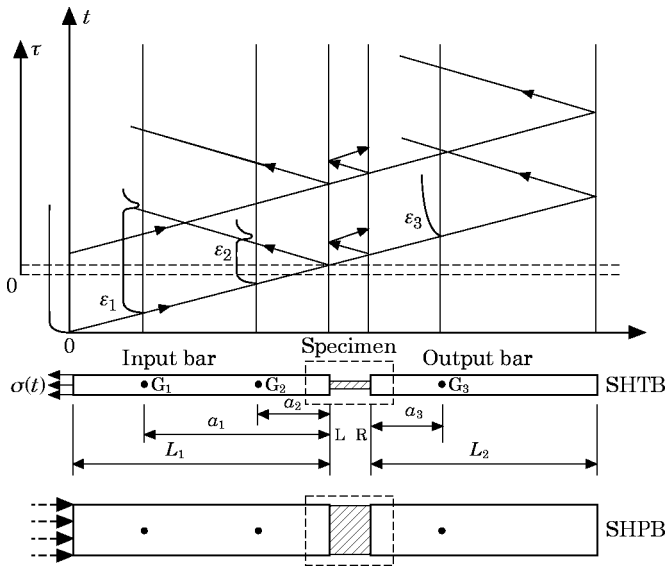

Figure 2. BTIA test system and SHPB test system and the Lagrange X-T sketch of their 1D experimental measuring principle. The shady part is the testing region of the specimen.

According to one-dimensional elastic stress wave theory, the stress $\sigma(t)$, strain $\epsilon(t)$ and strain rate $\dot{\epsilon}(t)$ in the specimen can be given [5]

$$\sigma(\tau) = \frac{EA}{2A_S}[\epsilon_i(\tau) + \epsilon_r(\tau) + \epsilon_t(\tau)], \qquad \epsilon(\tau) = \frac{C_0}{l_s}\int_0^\tau [\epsilon_i(\xi) - \epsilon_r(\xi) - \epsilon_t(\xi)]\,\mathrm{d}\xi,$$

$$\dot{\epsilon}(\tau) = (C_0/l_s)[\epsilon_i(\tau) - \epsilon_r(\tau) - \epsilon_t(\tau)], \tag{2, 3}$$

Because $\epsilon_i(\tau) + \epsilon_r(\tau) = \epsilon_t(\tau)$, formulae (1–3) can be simplified to

$$\sigma(\tau) = \frac{EA}{A_S}\epsilon_t(\tau), \qquad \epsilon(\tau) = \frac{2C_0}{l_s}\int_0^\tau [\epsilon_i(\xi) - \epsilon_t(\xi)]\,\mathrm{d}\xi, \qquad \dot{\epsilon}(\tau) = \frac{2C_0}{l_s}[\epsilon_i(\tau) - \epsilon_t(\tau)], \tag{4–6}$$

where A_s and l_s are the cross-section area and the length of the testing region (shown in Figure 2) respectively. C_0, A and E are the one-dimensional elastic stress wave speed, the cross sectional area and Young's modulus of the input/output bars respectively. $\epsilon_i(\tau)$, $\epsilon_r(t)$ are the incident strain signal and reflective strain signal in the input bar and $\epsilon_t(t)$ is the transmitted strain signal in the output bar measured by strain gauges respectively. The experimental data are analyzed by formulae (1–3) with three strain signals ($\epsilon_i(t)$, $\epsilon_r(t)$ and $\epsilon_t(t)$) and by formulae (4–6) with two strain signals ($\epsilon_i(t)$ and $\epsilon_r(t)$).

The specimen in BTIA is a dumb bell shaped cylindrical (see Figure 1), while in SHPB, it is a simple flat cylindrical like. This will make the stress wave propagation in the former system more complicated in two aspects: (1) there exist two non-homogeneous connecting regions composed of two kinds of materials (which form totally four physical and geometric discontinuous sections); (2) stress concentration in the roots of the testing region. Both aspects may cause certain deviation from the assumptions adopted in the 1D experimental measuring principle.

The theoretical demonstration of the validity of the experimental measuring principle for BTIA is more difficult than that of SHPB. It may include a lot of problems such as whether the experimental measuring principle can still be approximately valid or not, what the foundations making the experimental measuring principle valid are, how the specimen geometry affects the experimental results and how to reasonably select the specimen geometry in order to satisfy the foundations. It has to be resolved finally only through high dimensional dynamic numerical analysis.

In the present paper, first a two-dimensional axisymmetric finite element model for BTIA with a dumbbell-shaped cylindrical specimen made of an elastoplastic material is established. The numerical solution for the system under a stress impulse load on the left end-surface of the input bar is obtained by ADINA. In the scope of elastoplastic theory, the above mentioned theoretical problems can be answered by the numerical analysis.

The procession of demonstrating is as follows. First, the constitutive relation of the specimen material selected for the simulative analysis in advance is called the input constitutive relation. Second, through numerical solution of BTIA, the strain signals at the gauge positions on the input/output bar can be obtained. Using these strain signals, the three-wave predicted values or the two-wave predicted values of the stress $\sigma_0(t)$, strain $\epsilon_0(t)$ and strain rate $\dot{\epsilon}_0(t)$ of the specimen can be calculated respectively by the formulae (1–3) or formulae (4–6). Third, through the numerical solution, the average values of the stress, strain and strain rate in the middle of the testing region can be directly obtained, which is called the actual values of the stress, strain and strain rate of the specimen. Thus, through calculation, one gets two constitutive relations: the predicted one and actual one. By comparison of these two relations, the validity of the 1D experimental measuring principle can be demonstrated and discussed.

1.2. FINITE ELEMENT METHOD (FEM) AND PROGRAM ADINA

The finite element program for automatic dynamic incremental non-linear analysis (ADINA) [6, 7] is used for FEM analysis in the present paper. Here the implicit Newmark algorithm for integrating the governing equation with respect to time is employed. The spatially discretized equations of motion can be written as

$$[\mathbf{M}]\ddot{\mathbf{u}} + [\mathbf{K}]\mathbf{u} = \mathbf{f}, \tag{7}$$

where [**M**] is the total consistent mass matrix (the order of numerical integration is 3), [**K**] is the total stiffness matrix (the order of numerical integration is 2), u, $\ddot{u}$ are displacement and acceleration vectors respectively, and **f** is the external force vector.

In the implicit Newmark algorithm, the following assumptions are made

$$^{t+\Delta t}\dot{\mathbf{u}} = {}^{t}\dot{\mathbf{u}} + [(1-\delta){}^{t}\ddot{\mathbf{u}} + \delta\, {}^{t+\Delta t}\ddot{\mathbf{u}}]\Delta t,$$

$$^{t+\Delta t}\mathbf{u} = {}^{t}\mathbf{u} + {}^{t}\dot{\mathbf{u}}\Delta t + [(\tfrac{1}{2}-\alpha){}^{t}\ddot{\mathbf{u}} + \alpha\, {}^{t+\Delta t}\ddot{\mathbf{u}}]\Delta t^2, \tag{8, 9}$$

where α, δ are two parmeters to control the precision and stability of integration, and $\delta = 0{\cdot}54$, $\alpha = 0{\cdot}25\ (0{\cdot}5 + \delta)^2$ are selected.

In FEM analysis, the time step for integration is $\Delta t = 0{\cdot}1$ μs. Since the spatially discretized equation is non-linear, in order to assure the convergence and precision of the numerical solution, the total stiffness matrix is reformed and the equilibrium iteration is used in the process of solving discretized equations at each time step.

Because of the complexity of the above mentioned dynamic problem with several physical and geometric discontinuities, the feasibility of solving the problem by ADINA cannot be checked directly, but has to be checked indirectly. Several examples, including Betholf's analytical results of SHPB, is compared with the results of ADINA, which confirm the feasibility of ADINA. Details of this part can be seen in reference [8].

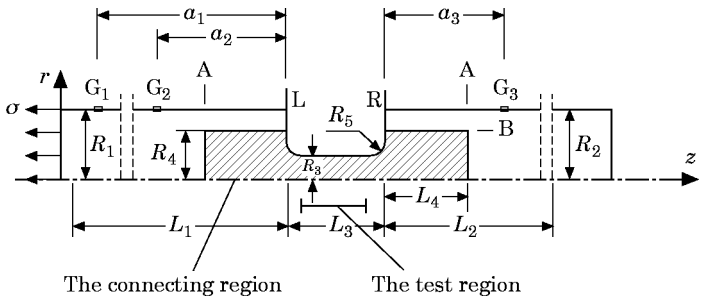

Figure 3. Two-dimensional axisymmetric model.

2. NUMERICAL SIMULATION AND ANALYSIS

2.1. FINITE ELEMENT MODEL

The BTIA system (shown in Figure 1) is simplified as a two-dimensional axisymmetric model (shown in Figure 3). G_1, G_2 and G_3 (shown in Figure 2) are three gauges on the input-output bars. The specimen is dumb bell shaped and cylindrical consisting of a testing region, two connecting regions and two additional transitional fillets at the roots. A stress impulse is uniformly applied on the end-surface of the input bar.

The stress on the right end-surface of the output bar and the other surfaces, i.e., the side surface and the surface at the varying sections (L and R), are free. The force equilibrium condition and the continuous displacement condition at internal interfaces (A and B) are satisfied. The model is stationary at initial time.

The meshes for the model shown in Figure 3 are composed of three groups i.e., the input bar, the specimen and the output bar. The input/output bars and the specimen are modelled respectively with 1500 and 300 four-noded, two-dimensional quadrilateral isoparametric elements. 60 three-noded, two-dimensional trilateral isoparametric elements are used to connect the meshes of different thickness.

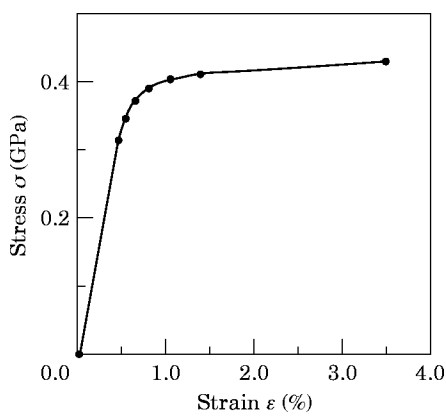

Figure 4. Constitutive relation of the specimen.

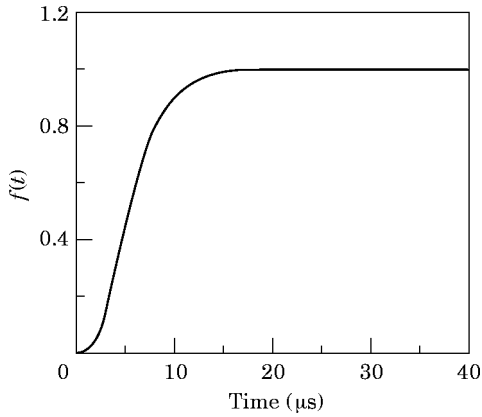

Figure 5. Impulse load function ($f(t)$).

The bars are made of a homogeneous isotropic linear elastic material. The Young's modulus (E), mass density (ρ) and Poisson ratio (v) of the input/output bars are 200 GPa, 8000 kg/m^3, 0·25 respectively. A strain rate independent material LY12cz aluminium alloy is chosen as the specimen material in the present paper to avoid the effects of strain rate. Its constitutive relation can be simplified to form a hardening model (see Figure 4), the 1D consitutive equation is

$$\sigma_y = \begin{cases} E\varepsilon & \sigma < \sigma_s \\ \sigma_s \varphi(\varepsilon) & \sigma \geq \sigma_s \end{cases} \tag{10}$$

TABLE 1

Geometric parameters of the model

	Input bar	Output bar	Testing region	Connecting region	Fillet
Length (mm)	$L_1 = 360$	$L_2 = 360$	$L_3 = 12$	$L_4 = 12$	
Radius (mm)	$R_1 = 6$	$R_2 = 6$	$R_3 = 1{\cdot}5$	$R_4 = 3$	$R_5 = 1$
Other parameters (mm)	$a_1 = 240$	$a_2 = 120$	$a_3 = 120$		

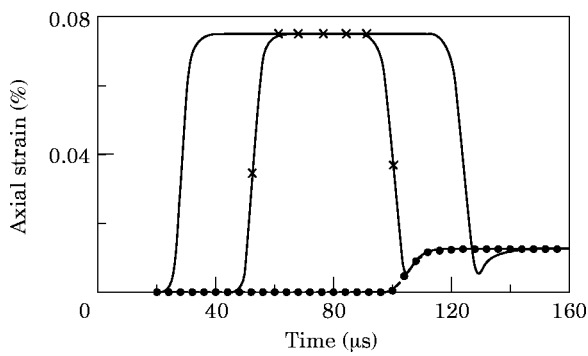

Figure 6. Strain signal on the input bar and output bars, with fillet.

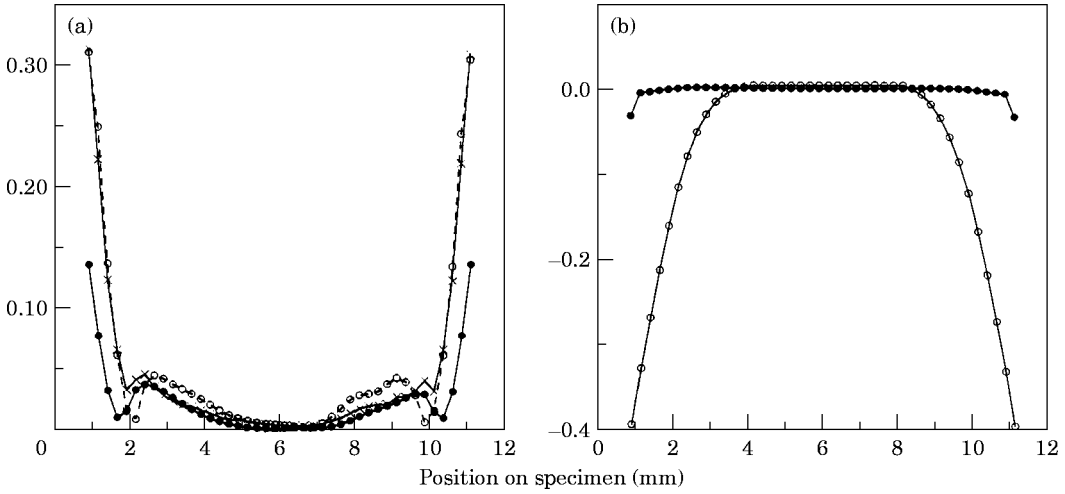

Figure 7. Uniformity of stress (strain) and the unidirectivity of stress in the testing region during the plastic process at $t = 120\,\mu s$ (test piece with fillet). Key: (a) –●–, $(\sigma_z^{max} - \bar{\sigma}_z)/\bar{\sigma}_z$; - - ○ - -, $(\varepsilon_z^{max} - \bar{\varepsilon}_z)/\bar{\varepsilon}_z$; —, max $\sigma_{ij}/\bar{\sigma}_z$: (b) –●–, $(\bar{\sigma}_z - \bar{\sigma}_z^{mid})/\bar{\sigma}_z^{mid}$; –○–, $(\bar{\varepsilon}_z - \bar{\varepsilon}_z^{mid})/\bar{\varepsilon}_z^{mid}$.

where $E = 70$GPa is Young's modulus, $\sigma_s = 0.3179$GPa is yield stress and $\varphi(\varepsilon)$ is a function of ε which increases as ε increases. The Poisson ratio of LY12cz is 0.3. The deviatoric stress s_{ij} is limited by the Von Mises yield condition.

As the incident impulse is very smooth, the applied impulse at the far end side of the input bar is selected as that with a smooth rise ($\sigma(t) = p_0 f(t)$) in which the amplitude $p_0 = 0.15$ GPa and $f(t)$ is shown in Figure 5.

Other geometric and physical parameters of the specimen are listed in Table 1. By solving the model with the implementation of ADINA, the strain signals (shown in Figure 11) at the gauge positions G_1, G_2 and G_3 can be obtained (see Figure 6).

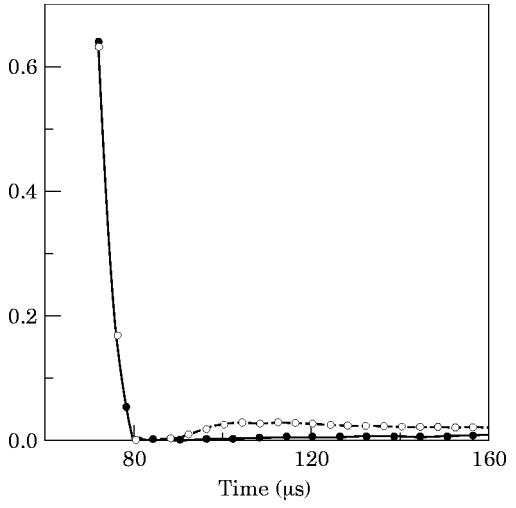

Figure 8. The uniformity of stress and strain with respect to time for specimen with fillet. Key: –●–, $(\bar{\sigma}_z^{max} - \bar{\sigma}_z^{tot})/\bar{\sigma}_z^{tot}$; - - ○ - -, $(\bar{\varepsilon}_z^{max} - \bar{\varepsilon}_z^{tot})/\bar{\varepsilon}_z^{tot}$.

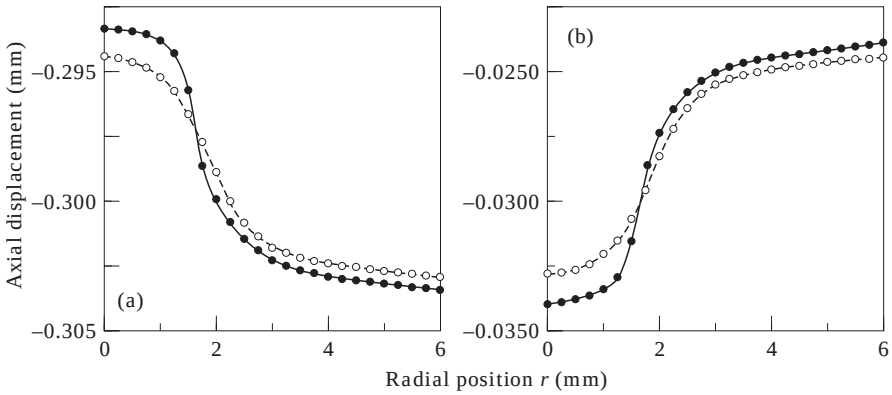

Figure 9. Displacement distribution on L and R cross-sections during the plastic process at $t = 120$ μs. (a) L cross-section; (b) R cross-section. Key: - - ○ - -, with fillet; –●–, without fillet.

2.2. DEMONSTRATION OF THE VALIDITY OF 1D EXPERIMENTAL MEASURING PRINCIPLE

2.2.1. *Stress and strain distribution in the testing region of the specimen with fillets*

The stress and strain distribution and the ratio of the maximum non-axial stress to the average axial stress in the testing region at $t = 120$ μs (when the testing region is in the plastic state and the strain value in the middle of testing region is about 2%) are summarized in Figure 7a. Where $\sigma_z^{\max}$ ($\epsilon_z^{\max}$) represent the maximum axial stress (strain), max (σ_r, σ_φ, τ_{rz}) represent the maximum non-axial stress on some cross-sections in the testing region, and $\bar{\sigma}_z(\bar{\epsilon}_z)$ represent the average stress (strain) in the corresponding cross-section. Figure 7a indicates that along the longitudinal direction, the values of $(\sigma_z^{\max} - \bar{\sigma}_z)/\bar{\sigma}_z$, max $(\sigma_r, \sigma_\varphi, \tau_{rz})/\bar{\sigma}_z$ and $(\epsilon_z^{\max} - \bar{\epsilon}_z)/\bar{\epsilon}_z$ in 85% of the testing region are less than 5%.

The ratios of the average axial stress (strain) in the testing region to the axial stress (strain) in the mid cross-section of the testing region at $t = 120$ μs are summarized in Figure 7b. Where $\bar{\sigma}_z(\bar{\epsilon}_z)$ represent the average axial stress (strain) on some cross-section in the testing region, $\bar{\sigma}_z^{\text{mid}}(\bar{\epsilon}_z^{\text{mid}})$ represent the average axial stress (strain) in the mid cross-section of the testing region. Figure 7b indicates that along the longitudinal direction, the value of $(\bar{\sigma}_z - \bar{\sigma}_z^{\text{mid}})/\bar{\sigma}_z^{\text{mid}}$ in 90% of the testing region is less than 5% and the value of $(\bar{\epsilon}_z - \bar{\epsilon}_z^{\text{mid}})/\bar{\epsilon}_z^{\text{mid}}$ in 75% of the testing region is less than 5%.

The uniformity of stress and strain in the testing region with respect to time is summarized in Figure 8. $\bar{\sigma}_z^{\max}(\bar{\epsilon}_z^{\max})$ represent the maximum average axial stress (strain) among various cross-sections in the testing region. $\bar{\sigma}_z^{\text{tot}}(\bar{\epsilon}_z^{\text{tot}})$ represent the average axial stress (strain) in the testing region. Figure 8 indicates that the axial stress (strain) distribution is non-uniform in the beginning microseconds after the stress wave approaches the testing region, while after several microseconds during which the wave reflects and transmits in the testing region, the distributions become uniform. Therefore, the non-uniformity of stress (strain) in the testing region hardly has any influence on the experimental results.

The analytical results in reference [8] show that the uniformity of stress and strain in the testing region is better when the latter is in the elastic state than when it is in the plastic state. The phenomenon can also be found in Figure 8. That is

because the elastoplastic interfaces exist in the roots of the testing region when the middle of the testing region is in the plastic state, which makes the stress wave propagation in the roots of the testing region very complicated. Bertholf's analytical results for the SHPB system [2] gave the same physical phenomenon as mentioned above. Rajendran and Bless [9] Cross and Bless [10] also gave the analysis and the explanation for the physical phenomenon.

As summarized in section 2.2.1., the stress and strain fields in the middle of the testing region (having a larger length to diameter ratio, i.e., $L_3/R_3 \geqslant 8$) are approximately uniform and under a unidirectional stress state. The axial stress is rather greater than the non-axial stresses. The non-uniform stress and strain region is only located in the roots of the testing region. In a word, the assumptions (i.e., the uniformity of stress and strain under a unidirectional stress state in the middle of testing region) in the experimental measuring principle can be approximately satisfied for the BTIA system with the specimen having a matching geometric sizes.

2.2.2. *Distortion of* L *and* R *cross-sections and the stress concentration in the roots of the testing region and its elimination*

Here, the model without fillets is also analyzed, and its numerical results are compared with the ones for the model with fillets.

2.2.2.1. Displacement distribution on the L and R cross-sections. Figure 9 shows the displacement distribution on the L and R cross-section at $t = 120$ μs and indicates that the distortion of the L and R cross-sections is remarkable for the specimen which has fillets, while the distortion becomes apparently weak for the specimen which has no fillets. The physical reasons causing the distortion are the severe geometric discontinuation in the roots of the testing region and the discontinuity material properties in the B interface (shown in Figure 1).

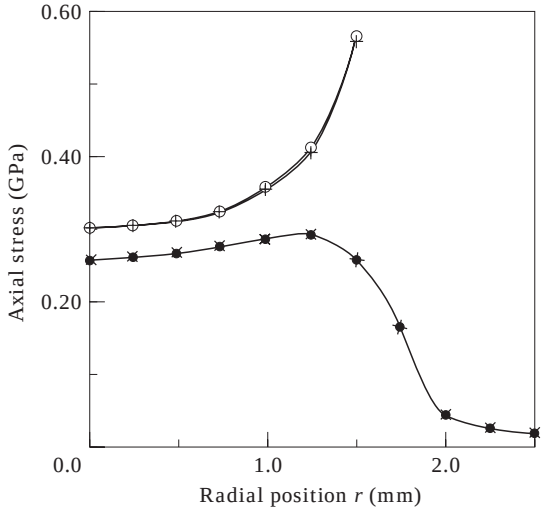

Figure 10. Stress distribution on L and R cross-sections during the plastic process at $t = 120$ μs. Key: ×, with fillet for L; ●, with fillet for R; ○, without fillet for L; +, without fillet for R.

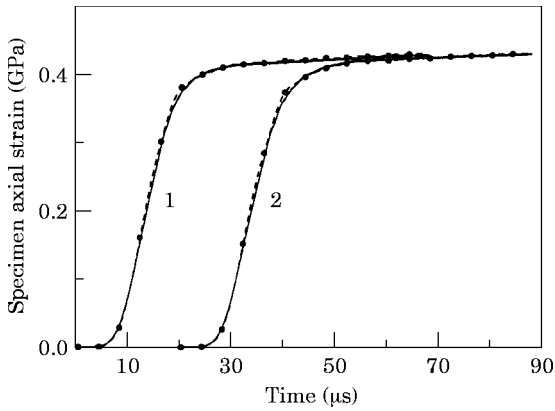

Figure 11. Specimen stress history. Key: 1, with fillet; 2, without fillet; —, actual strain; –●–, predicted strain.

2.2.2.2. Stress distribution on the L and R cross-sections. Figure 10 shows the stress distribution on the L and R cross-sections at $t = 120$ μs and indicates that dramatic stress concentration exists in the concave location of the roots of the testing region for the model without fillets, while for the model with fillets, the anomalous stress point and the stress concentration in the roots of the testing region disappear.

2.2.3. *Foundations of the validity of the assumptions in* 1D *experimental measuring principle*

The comparison of the actual values and the predicted values (stress, strain, and strain rate and constitutive relation) obtained by the experimental formula (4–6) for the specimen with fillets and without fillets are summarized in Figures 11–14.

Figure 11 shows that the predicted stress coincides well with the actual stress regardless of whether the specimen has fillets or not, which indicates that the fillets have little influence on the precision of the predicted stress.

Figure 12 shows that for the specimen without fillets, the predicted strain is greater than the actual strain and the difference becomes bigger as time increases, but for the specimen with fillets, the predicted strain is identical with the actual

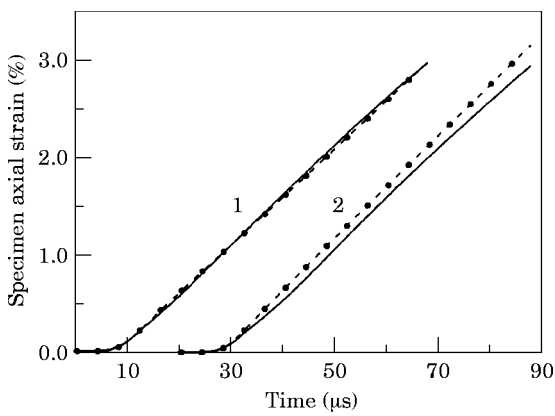

Figure 12. Specimen strain history. Key as for Figure 11.

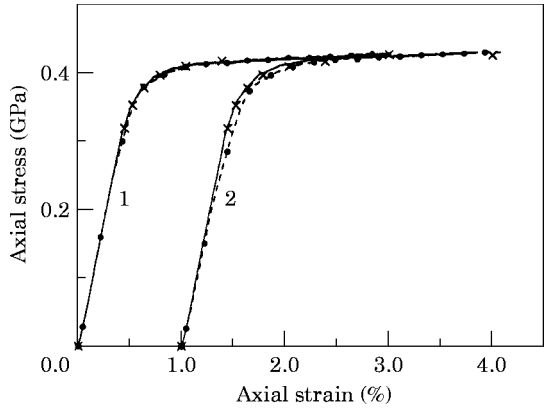

Figure 13. Specimen stress strain relation. Key as for Figure 11 plus ×, input.

strain. This is because the predicted strain is dependent on the relative displacements between the L and R cross-sections and the length of the testing region. If the specimen has no fillets, both the distortion on the L and R cross-sections and the relative displacements between them are slightly larger. Thus, in order to reduce the difference between the predicted strain and the actual strain, the distortion on the L and R cross-sections must be reduced (but the distortion cannot be eliminated completely) and the rigidity in the roots of the testing region must also be solidified to partially counteract the relative displacement between the L and R cross-sections. The way of adding the fillets in the roots of the testing region can achieve these above mentioned aims.

Figure 13 shows that the predicted constitutive relation coincides with the actual constitutive relation for the specimen with fillets, but an error (especially in the vicinity of yield points) is obvious for the specimen without fillets. Figure 14 indicates that the precision of the predicted strain rate for the specimen with fillets is better than the one without fillets, and the bar–bar tensile impact test can be considered as the dynamic test with a constant strain rate.

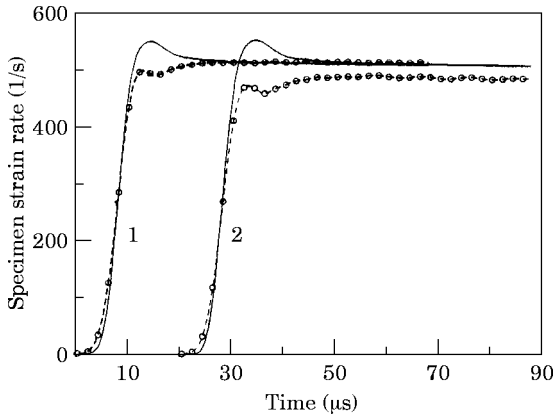

Figure 14. Strain-rate history. Key as for Figure 11 except - - ○ - -, predicted.

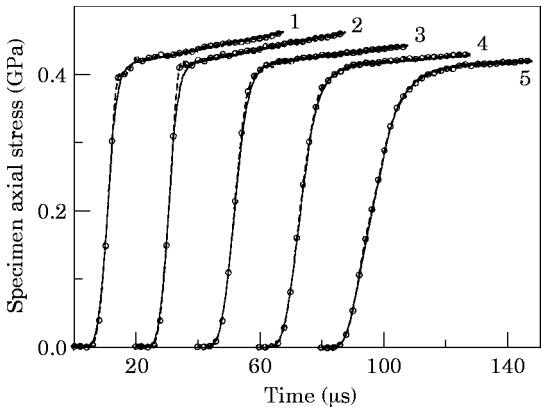

Figure 15. Specimen stress history. Key: —, actual; - - - -, predicted; 1, 1130/s; 2, 710/s; 3, 510/s; 4, 310/s; 5, 1130/s.

By way of changing the amplitude (p_0) in $\sigma(t) = p_0 f(t)$, the strain rates of simulative tests can be changed. For the above model with fillets, the BTIA testing processes of different strain rates are simulated by selecting respectively different amplitudes p_0 (i.e., 0·1 GPa, 0·15 GPa, 0·2 Gpa, 0·25 GPa and 0·3 GPa). The simulative experimental results are listed in Figures 15 and 16, in which curves 1, 2, 3, 4 and 5 are for the different amplitudes p_0 (i.e., 0·1 GPa, 0·15 GPa, 0·2 Gpa, 0·25 GPa and 0·3 GPa) respectively. Figures 15 and 16 show that the strain rate has little influence on the precision of the predicted stress, but the influence is concentrated mainly near the initial yield stress. Figure 16 also indicates that the strain rate hardly has any influence on the precision of the predicted strain.

In section 2.2, the complete process of the BTIA test has been numerically simulated by FEM. The foundations of the validity of the assumptions in the 1D experimental measuring principle has been demonstrated within the framework of elastoplastic theory. That is,

1. A uniform stress and strain region, existing within a unidirectional stress state, must be formed in the middle of the testing region.

2. By adding fillets in the roots of the testing region, the stress concentration in the roots of the testing region can be partially eliminated. Meanwhile, adding

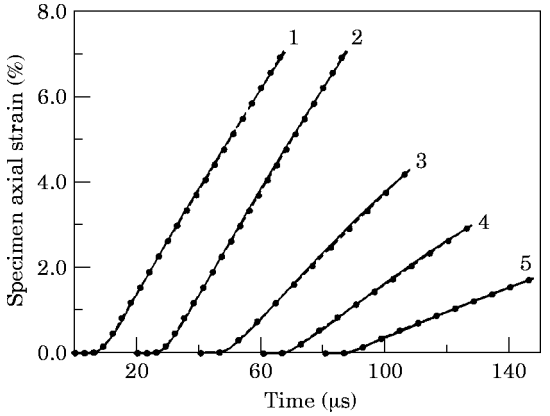

Figure 16. Specimen strain history. Key as for Figure 15 except - - ● - -, predicted.

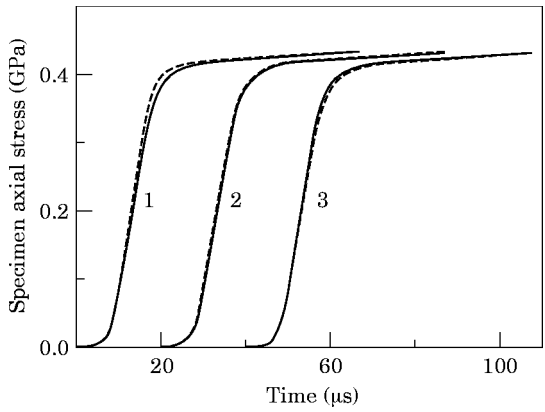

Figure 17. Specimen stress history. Key: 1, 20 mm; 2, 10 mm; 3, 0 mm; —, actual; - - - - , predicted.

fillets can debase the distortion of the L and R cross-sections, so as to reduce and counteract the relative displacement between them. Thus the precision of the predicted strain is improved.

3. The average value of stress and strain (the actual value) in the uniform middle of the testing region should coincide with the predicted value.

Changing specimen geometric parameters may cause violation from the above mentioned foundation. How to rationally select the specimen shape and how to connect the specimen with the input/output bars is now discussed in detail.

3. EFFECTS OF SPECIMEN'S GEOMETRIC SIZES ON EXPERIMENTAL RESULTS

In the discussion below, through changing some of the specimen's geometric sizes and keeping other sizes unchanged, the influence of the specimen's geometric sizes (L_3, R_3, L_4, R_4 and R_5) on the experimental results is studied. Other parameters such as the geometry and material properties of the input/output bar and the applied stress impulse, are the same as those in section 2.1.

3.1. EFFECT OF THE LENGTH (L_4) OF THE CONNECTING REGION ON THE EXPERIMENT RESULTS

In three cases, where the length (L_4) of the connecting region are (1) $L_4 = 20$ mm, (2) $L_4 = 10$ mm and (3) $L_4 = 0$ (i.e., without the connecting region) and other sizes are kept unchanged ($R_4 = 3$ mm, $L_3 = 12$ mm, $R_3 = 1{\cdot}5$ mm and $R_5 = 1{\cdot}0$ mm), the simulated results (the predicted value and the actual value) for the three cases are summarized in Figures 17 and 18, from which the following conclusions can be drawn.

1. The effects of L_4 on the predicted stress is mainly concentrated near the initial yield stress. Figure 17 shows the precision of the predicted stress is very high when $L_4 = 10$ mm. When $L_4 > 10$ mm, the error on the high side of the predicted stress relative to the actual stress increases as L_4 increases. When $L_4 < 10$ mm, the error decreases as L_4 decreases and may even yield a negative value. Especially for the specimen without the connecting region ($L_4 = 0$), the error is remarkable. The

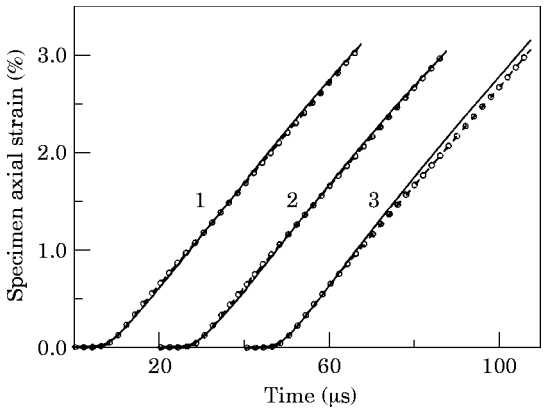

Figure 18. Specimen strain history. Key as for Figure 17 except - - ○ - -, predicted strain.

phenomena are caused by both the effects of the transverse and longitudinal inertia of the connecting and the testing regions.

2. In Figure 18, the effect of L_4 on the precision of the predicted strain is slight. It is because L_4 has hardly any influence on the deformation of the L and R cross-sections in a certain range of length. But especially for the case without the connecting region, the distortion of the L and R cross-sections is relatively small, and fillets in the roots of the testing region cause an excessive increase in its rigidity. Therefore, the predicted stress is smaller than the actual stress.

3.2. EFFECTS OF THE RADIUS (R_4) OF THE CONNECTING REGION ON THE EXPERIMENTAL RESULTS

In the three cases, where the radii (R_4) of the connecting region are (1) $R_4 = 4$ mm, (2) $R_4 = 3$ mm and (3) $R_4 = 0$ (i.e., without the connecting region) and keeping other sizes unchanged ($L_4 = 12$ mm, $L_3 = 12$ mm, $R_3 = 1{\cdot}5$ mm and $R_5 = 1{\cdot}0$ mm), the simulated results (the predicted value and the actual value) for these cases are summarized in Figures 19 and 20.

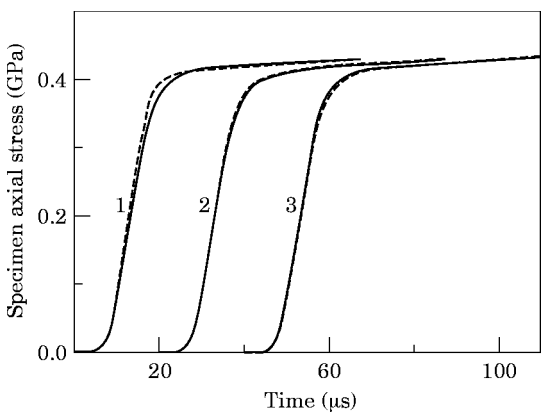

Figure 19. Specimen stress history. Key: 1, 4 mm; 2, 3 mm; 3, 0 mm; — actual; - - - , predicted.

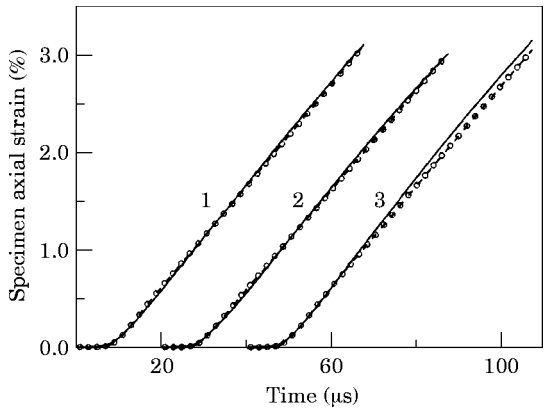

Figure 20. Specimen strain history. Key as for Figure 19 except - - ○- -, predicted strain.

From Figures 19 and 20, the same conclusions as those in section 3.2.1 can be drawn. It must be pointed out that the effect of R_4 on the precision of the predicted strain is slightly greater than that of L_4. It is because R_4 has certain influence on the distortion of the L and R cross-sections.

3.3. INFLUENCES OF THE LENGTH (L_3) OF THE TESTING REGION ON THE EXPERIMENTAL RESULTS

In the three cases, where the length (L_3) of the testing region are respectively (1) $L_3 = 9$ mm, (2) $L_3 = 12$ mm and (3) $L_3 = 15$ mm and other sizes are kept unchanged ($L_4 = 12$ mm, $R_4 = 3$ mm, $R_3 = 1{\cdot}5$ mm and $R_5 = 1$ mm), the simulated results (the predicted value and the actual value) are summarized in Figures 21 and 22, from which the following conclusions can be drawn.

1. As shown in Figure 21, over part of the range of the length (L_3) and also part of the range of the radius (R_3), L_3 plays a minor role in the precision of the predicted stress. It is because in the appropriate range an approximate uniform stress and strain region under a unidirectional stress state can be formed in the middle of the testing region. $L_3 = 12$ mm and $L_3 = 15$ mm are in the applicable

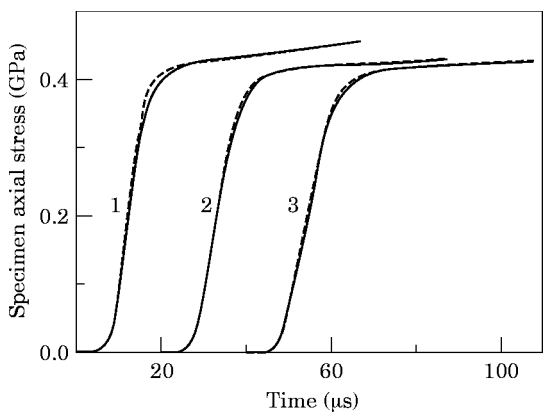

Figure 21. Specimen stress history. Key: 1, 9 mm; 2, 12 mm; 3, 15 mm; —, actual; - - - , predicted.

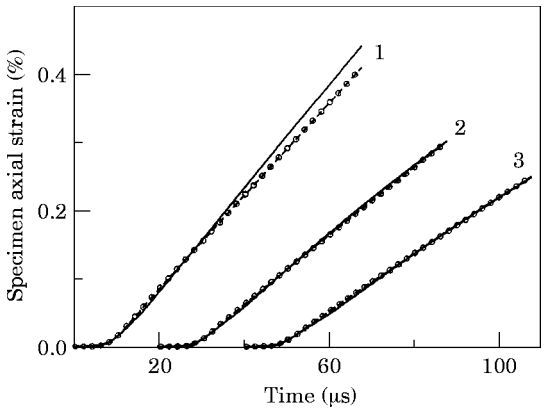

Figure 22. Specimen strain history. Key as for Figure 22 except - - ○- -, predicted.

range. Beyond the applicable range, there is a certain difference between the predicted stress and actual stress. For testing regions which are too short (for example $L_3 = 9$ mm), the transverse constraint in the roots of the testing region undermine severely the uniformity of stress and strain in the testing region, which destroys the foundations of the experimental measuring principle. While for testing regions, which are too long, the bigger longitudinal inertia of the testing region can cause oscillation of the stress time curve, which in turn reduces greatly the precision of the predicted stress.

2. Figure 22 shows that the length (L_3) plays an important role in the precision of the predicted strain. It is because the predicted strain is directly dependent on L_3, but the distortion of the L and R cross-sections is almost independent of L_3 and is controlled by other specimen dimensions.

3.4. EFFECTS OF THE RADIUS (R_3) OF THE TESTING REGION ON THE EXPERIMENTAL RESULTS

In the three cases, where the radii (R_3) of the testing region are respectively (1) $R_3 = 2$ mm, (2) $R_3 = 1{\cdot}5$ mm and (3) $R_3 = 1$ mm and the other sizes are kept

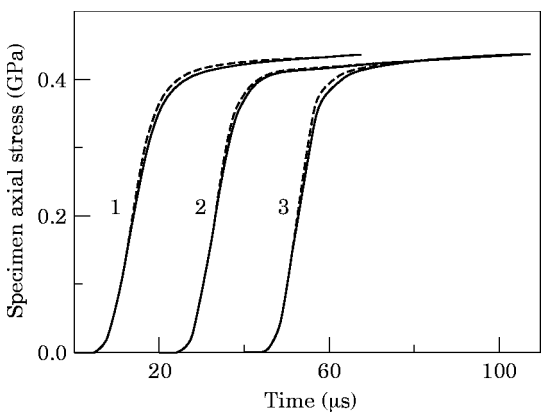

Figure 23. Specimen stress history. Key: 1, 2 mm; 2, 1·5 mm; 3, 1 mm. —, actual; - - - , predicted.

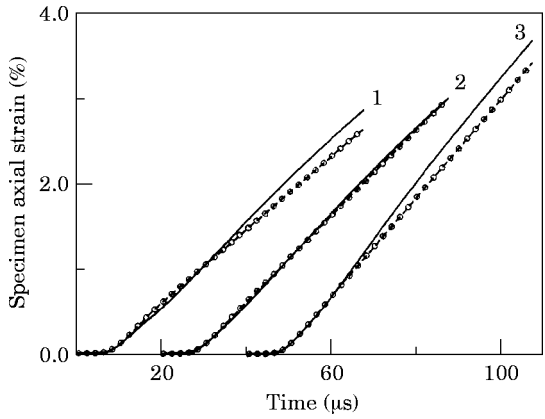

Figure 24. Specimen strain history. Key as for Figure 23 except - - ○- -, predicted.

unchanged ($L_4 = 12$ mm, $R_4 = 3$ mm, $L_3 = 12$ mm and $R_5 = 1$ mm), the simulated results (the predicted value and the actual value) for the three cases are summarized in Figures 23 and 24.

The following conclusions can be drawn from Figures 23 and 24.

1. From Figure 23, it can be seen that for a certain range of the radius (R_3) and also for a certain range of the length (L_3), an approximate uniform stress and strain region under a unidirectional stress state in the testing region can be formed exactly. In the applicable range, the radii (R_3) slightly influence the precision of the predicted stress, and the influence is determined by the synthetic effects of the transverse and longitudinal inertia of the connecting and testing regions, i.e., by the matching relation between the geometric sizes of the specimens.

2. Figure 24, shows that the radius (R_3) plays an important role in the precision of the predicted strain. The uniformity in the testing region under the uniaxial stress state becomes very weak if the testing region has a larger radius (for example $R_3 = 2$ mm), which makes the predicted strain lower than the actual strain. But if R_3 is too small (for example $R_3 = 1$ mm), the radius of the fillets (R_5) may seem relatively larger, which, as will be seen in the next section (section 3.5), can make the predicted strain lower than the actual strain.

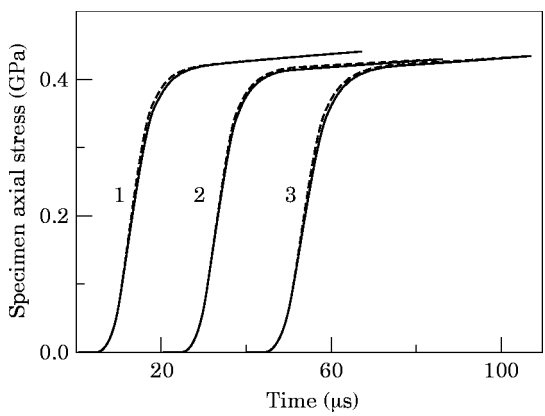

Figure 25. Specimen stress history. Key: 1, 1·5 mm; 2, 1 mm; 3, 0 mm. —, actual; - - - , predicted.

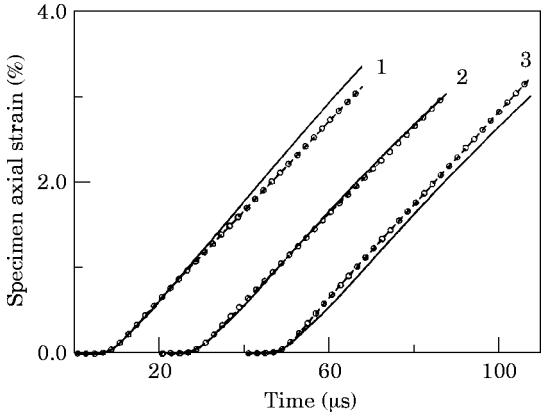

Figure 26. Specimen strain history. Key as for Figure 23 except - - ○- -, predicted.

3.5. INFLUENCES OF THE RADIUS (R_5) OF THE FILLETS ON THE EXPERIMENTAL RESULTS

In the three cases, where the radii (R_5) of the fillets are respectively (1) $R_5 = 1{\cdot}5$ mm, (2) $R_5 = 1$ mm and (3) $R_5 = 0$ (i.e., without fillets in the roots of the testing region) and the other sizes ($L_4 = 20$ mm, $R_4 = 3$ mm, $L_3 = 12$ mm and $R_3 = 1{\cdot}5$ mm) are kept unchanged, the simulated results (the predicted value and the actual value) for the three cases are summarized in Figures 25 and 26.

The following conclusions can be drawn from Figures 25 and 26.

1. Figure 25 shows the radius (R_5) of fillets influences slightly the precision of the predicted stress. It is because R_5 only influences the stress distribution in the roots of the testing region and hardly influences the uniformity of stress and strain under a undirectional stress state in the middle of the testing region.

2. Figure 26 shows R_5 has a remarkable effect on the precision of the predicted strain. If the radius (R_5) of the fillets is too large, the predicted strain is smaller than the actual strain; otherwise, the predicted strain is greater than the actual strain. It is because the effect of R_5 is to eliminate the increase of the relative displacement between the L and R cross-sections caused by the distortion of the L and R cross-sections. But excessive elimination can occur if R_5 is too big, while conversely insufficient elimination can occur if R_5 is too small.

As summarized from section 3, the connecting region has remarkable influences on the predicted stress, and the influence is dependent on the testing region to a certain extent. The predicted stress can reach a high enough precision if the matching relation between the specimens' geometric sizes is found. The matching relation is to ensure the formation of the approximate uniform uniaxial stress region in the middle of the testing region. The fillets and the testing region play a main role in the predicted strain. Therefore, one can rationally adjust the specimens' geometric sizes to eliminate and counteract the various effects caused by the complicated stress wave propagation in the connecting region and in the roots of the testing region, in order to ensure high enough precision of the predicted stress.

In short, through adjusting the geometric parameters (L_4, R_4, L_3, R_3 and R_5), a rational matching relation among the parameters can be found and the matching relation is not unique. That is, in a certain range of specimen's geometric sizes, the precision of the predicted results is within the range of engineering error.

4. CONCLUSIONS AND RECOMMENDATIONS

The present paper demonstrates the validity of the experimental measuring principle in the scope of elastoplastic theory. So long as certain matching relation between the specimen's geometric parameters and the BTIA system is satisfied, the experimental measuring principle is always valid. If a correct matching relation is selected, the constitutive relation of the specimen material can be effectively obtained by the BTIA test. A detailed analysis of the problems of how to select a matching relation can be found in reference [8].

Because in real experiments the screw connection of the specimen with the bars cannot be perfect as has been described in the numerical analysis in this paper, the author's group have also developed a glued connection, in which the specimen is a dumb bell shaped flat one and is glued to the input/output bars. A numerical analysis of this system can be seen in another paper of the authors.

ACKNOWLEDGMENT

The research work in the present paper was supported by National Natural Science Foundation of the People's Republic of China.

REFERENCES

1. H. Kolsky 1949 *Proceedings of the Physical Society* Series **B 62**, 676–700. An investigation of the mechanical properties of materials at very high rates of loading.
2. L. D. Bertholf 1974 *Journal of Applied Mechanics* 137–144. Feasibility of two dimensional numerical analysis of the Split–Hopkinson Pressure Bar System.
3. L. D. Bertholf and C. H. Karnes 1975 *Journal of the Mechanics and Physics of Solids* **23**, 1–19, Two-dimensional analysis of the Split–Hopkinson Pressure Bar System.
4. Y. M. Xia *Journal of the National Natural Science Foundation of the People's Republic of China* **92**, No. 030. Science and technology achievement appraisal—rotating disc bar–bar tensile impact test apparatus and its experimental technique.
5. Y. M. Xia, X. Wang and B. C. Yang 1996 *Composites Science and Technology* **56**, 155–160, Constitutive equation for unidirectional composites under tensile impact.
6. K. J. Bathe 1982 *Finite Element Procedures in Engineering Analysis*. Englewood Cliffs, N.J.: Prentice-Hall.
7. K. J. Bathe 1981 *Massachusetts Institute of Technology*, *Cambridge*, *MA*. *Reports* AE81-1, AE81-2, AE81-3. ADINA—a finite elment program for automatic dynamic incremental nonlinear analysis.
8. C. Y. Wang 1996 *Ph.D. Thesis*, *University of Science and Technology of China*. Dynamic numerical analysis for bar–bar tensile impact testing system—demonstration for experimental measuring principle and matching relation among specimen's geometric sizes.

9. A. M. Rajendran and S. J. Bless 1986 *Experimental Mechanics* 319–323. Determination of tensile flow stress beyond necking at very high strain rates.
10. L. A. Cross and S. J. Bless 1984 *Experimental Mechanics* 184–186. New technique to investigate necking in a tensile Hopkinson bar.
11. C. Y. Wang and Y. M. Xia 1996 *Journal of China University of Science and Technology* **26**, 64–69. Two-dimensional finite element analysis of elastic wave propagation in cylindrical bars with interfaces.